Geomorphic process signatures reshaping sub-humid Mediterranean badlands: 1. Methodological development based on high-resolution topography

Llena Manel (Orcid ID: 0000-0001-7095-6188)

Smith Mark William (Orcid ID: 0000-0003-4361-9527)

Wheaton Joseph Michael (Orcid ID: 0000-0002-8361-8150)

Geomorphic process signatures reshaping sub-humid Mediterranean badlands: 1. Methodological development based on High Resolution Topography

Llena, M.[1,*], Vericat, D.[1,2], Smith, M.W.[3], Wheaton, J.M.[4]

[1] Fluvial Dynamics Research Group, Department of Environment and Soil Sciences, University of Lleida, Lleida, Spain.

[2] Forest Science and Technology Centre of Catalonia, Solsona, Spain.

[3] School of Geography, University of Leeds, Leeds, UK.

[4] Department of Watershed Sciences, Utah State University, Logan, USA.

* Corresponding author: mllena@macs.udl.cat

This article has been accepted for publication and undergone full peer review but has not been through the copyediting, typesetting, pagination and proofreading process which may lead to differences between this version and the Version of Record. Please cite this article as doi: 10.1002/esp.4821

Abstract

High Resolution Topography data sets have improved the spatial and temporal scales at which we are able to investigate the landscape through the analysis of landform attributes and the computation of topographic changes. Yet, to date, there have been only limited attempts to infer key geomorphic processes in terms of contributions to shaping the landscape. Highly erodible landscapes such as badlands provide an ideal demonstration of such an approach owing to the rapid changes observed over a relatively short time frame. In this technical note we present the Mapping Geomorphic Processes in the Environment (MaGPiE): a new algorithm that allows mapping of geomorphic process signatures through analysis of repeat High Resolution Topography data sets. The method is demonstrated in an experimental badland located in the Southern Central Pyrenees. MaGPiE is a GIS-based algorithm that uses as input: (a) terrain attributes (i.e. Slope, Roughness and Concentrated Runoff Index) extracted from Digital Elevation Models (DEM), and (b) a map of topographic changes (DEM of Difference, DoD). Initial results demonstrate that MaGPiE allows the magnitude and the spatial distribution of the main geomorphic processes reshaping badlands to be inferred for the first time.

Key words: Geomorphic process signatures, badlands, Structure from Motion, Topographic Changes, Mapping Geomorphic Processes in the Environment algorithm (MaGPiE).

1. INTRODUCTION

The proliferation of High Resolution Topography data sets, driven by the development of new surveying platforms (e.g. Unmanned Aerial Vehicles, UAVs), sensors (e.g. High Resolution Multispectral Cameras) and algorithms (e.g. Structure from Motion photogrammetry, SfM) has permitted quantification of topographic changes at unprecedented spatial resolutions over a wide range of temporal and spatial scales (see, for example, reviews in Passalacqua et al., 2015; Smith et al., 2015; Tarolli, 2014; Vericat et al., 2017). SfM-based topography has reduced substantially the cost involved in surveying. SfM may provide data sets at equivalent resolution and precision than other more-expensive surveying methods such as Terrestrial Laser Scanning (e.g. Carrivick and Smith, 2018; Smith and Vericat 2015; Westoby et al., 2012). Additionally, depending on the platform used to acquire the photographs, SfM allows large spatial scales to be surveyed in a short time, allowing the reconstruction of landscape topography at temporal scales that were difficult to reach before. High-frequency surveying has the potential to describe short-term controls on geomorphologic changes and more accurate analysis of processes (e.g. Cucchiaro et al. 2019; Williams et al. 2018). Therefore, we are now capable of acquiring detailed facsimiles of the landscape before and after disturbances, quantifying changes in form and, from these, we may infer the main reshaping geomorphic processes.

Badlands are described as highly dissected landscapes with steep hillslopes in soft rock outcrops or unconsolidated sediments and regolith, with little or no vegetation, being useless for agriculture (Gallart et al., 2002; Yair et al., 1980). Badlands are highly erodible with rapid erosion rates and high sediment yields (Bryan and Yair, 1982; Clotet et al., 1987) that make disproportionately large contributions to catchment scale sediment budgets (e.g. López-Tarazón et al., 2012; Nadal-Romero and Regüés, 2010) with potential negative effects on the downstream channel network (e.g. clogging, Buendía et al., 2013; Piqué et al., 2014) and infrastructure (e.g. reservoir siltation; Baade et al., 2012; Martínez-Casasnovas and Poch, 1998; Mueller et al., 2010). In general, surface features result from the interaction between highly erodible materials (soft or unconsolidated) with multiple geomorphological processes acting at different temporal and spatial scales (Moreno-de las Heras and Gallart, 2018; Nadal-Romero and García-Ruiz, 2018). The main factors controlling badland development are lithology, rainfall, temperature, vegetation cover, human activities and the degree of

connectivity, that is directly related to main landform attributes such as topography and roughness (Clarke and Rendell, 2010; Faulkner, 2008). Ultimately, geomorphic processes in such environments are determined by the interactions of these factors.

Topographic changes in badlands are generally estimated from sparse observations across relatively small scales (e.g. erosion pins in Barnes et al., 2016; Benito et al., 1992; Sirvent et al., 1997; experimental plots in Nadal-Romero et al., 2007; Regüés et al., 1995). High Resolution Topography offers the opportunity of examining topographic changes in a spatially-distributed way at multiple temporal and spatial scales. During the last decade several authors have used these data sets to monitor topographic changes in badlands (e.g. Ferrer et al., 2017; Nadal-Romero et al., 2015; Neugirg et al., 2016; Nobajas et al., 2017; Smith and Vericat, 2015; Stöcker et al., 2015; Vericat et al., 2014). Although these studies have greatly improved the quantification of rates of erosion or deposition and sediment yields, to our knowledge there has yet to be an attempt to further interrogate the rich data sets and quantify the magnitude and spatial distribution of the changes in form in relation to main geomorphic processes. There is a knowledge gap related to mapping geomorphic process signatures in a quantified manner to determine their spatial and temporal variability. Such maps will help to infer the magnitude of the main geomorphic processes controlling sediment export, landscape changes and evolution, and would help to prioritise and target catchment management practices aimed at reducing sediment yields. In this methodological note, we present the Mapping Geomorphic Processes in the Environment (MaGPiE) algorithm: MaGPiE facilitates the quantitative mapping of main geomorphic process signatures through analysis of repeat SfM-based High Resolution Topography data sets. We first present the MaGPiE algorithm followed by its application in an experimental badland landscape in the Southern Central Pyrenees.

2. THE MaGPiE ALGORITHM

MaGPiE is a GIS-based algorithm that uses as input: (i) terrain attributes extracted from Digital Elevation Models (DEM), and (ii) a map of topographic changes obtained via DEM of Difference (DoD). Therefore, DEMs before and after topographic changes are required. In general, main geomorphic process signatures are first identified, together with their main

characteristics in terms of both spatial extent and the magnitude and sign of the topographic changes associated with these. The inputs are then combined to provide the signatures that infer each process. Finally, a decision tree algorithm is applied to map the geomorphic processes on a cell-by-cell basis. The complete MaGPiE workflow is presented in Figure 1 and explained below.

Step 1. Identification of Main Geomorphic Process Signatures. We have combined a literature search and field observations to identify and classify the most relevant geomorphic process signatures that can be observed in badlands, the focus of this MaGPiE demonstration. A similar exercise would be needed to apply the MaGPiE algorithm in other geomorphologic landscapes in which main processes may differ to those identified here. In the case of sub-humid badlands, dominant geomorphic processes were divided into two main groups: (a) weathering-based processes and (b) erosional-based processes. Erosional processes are split between overland-flow and mass movement driven processes (following Barnes et al., 2016; Bryan and Yair, 1982; Clotet et al., 1987; Gallart et al., 2002; Huggett, 2011; Nadal-Romero and Regües, 2010; Nadal-Romero and García-Ruiz, 2018; Moreno-de las Heras and Gallart, 2018). Despite this classification, badlands are complex landscapes in which the interaction between (i.e. overlapping) geomorphic processes is often present (e.g. Vergari et al., 2019). In our case we have considered overlapping processes those that cannot be classified as any of the other identified. We are aware that the overlapping processes class may also include other processes not identified as the main geomorphic process signatures. The main overlapping geomorphic process signatures in the study area were *Sheet Washing* and *Regolith Cohesion Loss*, which take place mainly in areas with low slope and high exposure.

Table 1 shows the main badland geomorphic processes that are possible to be inferred from their signatures based on terrain attributes and changes in form. The table also presents the main drivers and some references in which these specific processes are described. In that way, a total of 6 specific geomorphic processes were identified: (1) *Sheet Washing*; (2) *Rilling and Gullying*; (3) *Cutting and Filling*; (4) *Mass Wasting* (5) *Regolith Cohesion Loss*; and (6) *Overlapping Processes*.

It is worth mentioning that sub-surface geomorphic processes (i.e. pipping) were not taken into account here because these are not acting in Eocene marls such as the ones observed in the experimental badlands. Even so, changes in form associated with these processes may be dominant in other environments (e.g. Faulkner, 2018; Gutiérrez et al. 1997), requiring consideration in the identification of main geomorphic process signatures in such environments.

Step 2. Preparing Inputs: landform attributes & topographic changes

Following Wheaton et al. (2013), we consider a geomorphic process signature arise when a distinct main process leads to a consistent topographic change, being also characterised by specific landform attributes. A total of three landform attributes (Slope, Roughness and a new developed Concentrated Runoff Index) extracted from the second (or 'new') DEM are used alongside the DoD to define key signatures of each geomorphic process.

The local Slope was selected as an input because is considered one of the main parameters that determine (slope) stability, and consequently, triggering mass movements (Bishop and Morgenstern, 1960; Morgenstern and Price, 1965). In the same way, Slope is also a main factor determining the distribution of erosional landforms associated with concentrated-fluxes (e.g. rills, gullies, channels; Gallart et al., 2002). Usually, the erosional stream landform size is negatively correlated with the slope and positively correlated with the upslope catchment area. Thus, Slope was used to differentiate between the processes that took place in steep areas (e.g. erosion caused by *Mass Wasting* and by *Rilling and Gullying*) and those occurring in relatively flat areas (e.g. *Regolith Cohesion Loss*, *Sheet Washing*). Slope is defined here as the maximum rate of change in elevation from each cell to its neighbours.

Several authors (e.g. Gallart et al., 2002; Regüés and Torri, 2002; Römkens et al., 2001) reported that Roughness is one of the main landform attributes that determines erosion and a range of geomorphic processes. Roughness values help to discern between deposition in main channels caused by in-channel processes (i.e. *Filling*) and deposition caused by lateral *Mass Wasting*, with the latter exhibiting higher roughness values (based on field observations; see some examples in figures of section 3.3). Roughness is defined as the mean

of the detrended standard deviation of the elevations within regular grid cells (see specific details in section 3).

The Topographic Wetness Index (TWI), a quantification of the topographic control on hydrological processes, is considered as a proxy of the concentrated surface water fluxes (Ali et al., 2014; Beven and Kirkby, 1979). Although the relation between slope and upslope area on which TWI is based has been used to discern between concentrated (i.e. channel) and diffuse (i.e. slope) processes (e.g. Roering et al. 2001; Vergari et al. 2019; Willgoose et al., 1991), it assumes a fully connected hydrological system. Badlands, however, can present different degrees of disconnectivity. In order to overcome this limitation, we have developed the Concentrated Runoff Index (CRI), a landform attribute based on a modification of the TWI. The CRI takes into account not just the magnitude of the TWI but also the Planform Curvature (PC). We assume that concave surfaces reflect more locally connected areas than convex areas. The CRI was calculated by means of the expression TWI+(PC×-1); where the TWI was computed as $\ln(A/\tan\beta)$, A is referred to the upslope area of a given cell (m^2), and β is the local gradient (in degrees). PC represents the normalised (from -1 to 1) planform curvature value obtained from the most recent DEM. The values were normalized by this range in order to not dominated the signal and only affect in those cases in which the TWI was very close to the threshold between concentrated and diffuse. Normalised PC values are multiplied by -1 in order to invert the sign of concave and convex surfaces. In that way, concave surfaces will be positive while convex surfaces will be negative, having an additive and subtractive weight on the TWI. The CRI was used to distinguish between overland flow processes caused by concentrated runoff (e.g. rills, gullies and channels, from small to big size), and those caused by diffuse runoff (e.g. *Sheet Washing*).

Finally, topographic changes were obtained by the comparison of the DEMs between surveys (the DoD). The old DEM is subtracted from the new DEM, where negative values indicate surface lowering or erosion and positive values indicate surface raising or deposition. It is important to note that negative and positive DoD values do not imply always erosion and sedimentation. For instance, in the case of the *Regolith Cohesion Loss*, the elevation of the surface increases when the old and the new DEMs are compared, but this is not related to any depositional process occurred during the study period. In this case physical weathering controls the expansion of the regolith (e.g. so-called '*popcorn'* features) in relation to climate

and geological conditions (e.g. Gallart et al., 2002; Kasanin-Grubin, 2013; Nadal-Romero and Regüés, 2010). The DoD is calculated using the Geomorphic Change Detection (GCD) extension for ArcMap (available at http://gcd.joewheaton.org/; see Wheaton et al., 2010) which has the advantage of incorporating uncertainty analysis based on minimum Level of Detection (minLoD), propagated errors or probabilistic thresholding.

Step 3. Defining the combination of landform attributes and topographic changes for each Geomorphic Process signature.

An expert-map of the main geomorphic process signatures is first elaborated examining i) topography; ii) orthomotomosaics; and iii) oblique photographs taken from a trail camera. The 90% of the mapped process signatures are used to (a) establish the thresholds of the classes of each attribute and DoD, and (b) to define the signatures (i.e. combination of classes) of each geomorphic process. The remaining 10% of the processes mapped in the field are used for validation of the classification.

Each landform attribute was divided in two classes: high and low in case of roughness and slope; or diffuse flow and concentrated flow in case of the Concentrated Runoff Index. DoD values are divided into four classes: high lowering, low lowering, low raising and high raising. The thresholds of each class and their combinations are based on the distribution of the values of the landform attributes and DoD per each geomorphic process. In the case of the landform attributes, the median value of each attribute was calculated across the whole DEM. These values will determine the class boundaries. In order to assign each geomorphic process signature to a class, the median value of the same attribute for cells classified into each geomorphic process is then compared with the class ranges and categorised accordingly (see example in Figure 1). In case of the thresholds for the DoD values, 0 defines the division between surface lowering and raising classes, while the 90^{th} and 10^{th} percentiles of the DoD values define the thresholds between high and low raising and lowering, respectively. Again, once the thresholds were established, the median DoD values in each process were analysed to classify each process. The expert-map identification of thresholds and combinations of attributes and DoD classes has been chosen to decrease the subjectivity and to allow a

validation of the results. The class boundaries and combinations identified for each geomorphic process are now described below.

In the case of Slope, two classes were defined: High Slopes (>45°) and Medium to Low Slopes (<45°). The selected threshold of 45° allows us to: (i) identify steep areas in which mass movements can be observed (e.g. *Mass Wasting*); and (ii) discern between concentrated runoff processes in rills and gullies (i.e. *Rilling and Gullying*) and those observed in the main channel (i.e. *Cutting and Filling*). These thresholds are agreement with Zhang et al. (2017) who identified the slope gradient of 47% to be the threshold value of increasing runoff and associated soil loss.

Roughness was grouped in two classes: High Roughness (>0.03 m) and Low Roughness (<0.03 m). In particular, regolith deposits coming from mass movements (e.g. *Mass Wasting*) tend to have a higher roughness than the values observed in deposits coming from overland-flow processes (e.g. *Sheet Washing, Cutting and Filling*). Gallart et al. (2002) described that in steep badlands hillslopes, unestablished regolith mass may fall towards the valley bottom with a consequent coarser roughness than the regolith transported by the channel system.

CRI was divided in two groups, a value of 1 was selected as a threshold between Diffuse flow (CRI<1) and Concentrated Flow (CRI>1), with the latter being mainly attributed to *Rilling and Gulling* and *Cutting and Filling* processes. Recently, Jancewicz et al. (2019), stated that the thresholding of TWI from the mean value plus standard deviation helps to recognize pathways of water and possible sediment transfer (i.e. concentrated flow). Similarly, here we have used the curvature to modify the results provided by the TWI when values are very close to the threshold between concentred and diffuse flows.

Finally, the DoD was grouped into four classes: High Lowering (<-0.15 m), Low Lowering (-0.15 – 0 m), Low Raising (0 – 0.07 m) and High Raising (>0.07 m). These values are in agreement with the average values of topographic changes observed in sub-humid badlands developed on marls for similar study periods (i.e. less than one year; Clarke and Rendell, 2010; James et al., 2017; Mathys et al., 1996; Nadal-Romero and Regüés, 2010; Smith and Vericat, 2015; Vericat et al., 2014). However, it is worth mentioning that the thresholds between these classes will depend on the considered time span and require what re-evaluation if the survey interval is altered.

The combination of these classes provides a unique signature or combination per each process. The inset table in Figure 1 shows the combined signatures of each process. For instance, the signature that defines surface lowering caused by *Rilling and Gullying* is: High Slope, High or Low values of Roughness, Concentrated Flow (High CRI) and either High or Low surface lowering. Therefore, a pixel that has all these inputs will be characterised as lowering potentially caused by *Rilling and Gullying*. It is worth to mention that in our case we have considered *Overlapping Processes* those yielding a distinct signature to the other identified processes.

Finally, the accuracy of the classes was estimated by a confusion matrix calculated following the method described by Chuvieco (2016). In this way, the 10% of the expert-mapped processes are used as training areas. These areas are compared with the MaGPiE results to assess the percentage agreement between observed and MaGPiE-based process as a measure of the accuracy of the classification. The results of the confusion matrix also allow to identify which processes were most reliable and which were more confused based in the classification results.

Step 4. Mapping Geomorphic Process Signatures

Once the thresholds of the classes of all inputs were defined, the classified rasters were combined in a multiband raster: a single data set in which each pixel has associated the different combinations of the input data sets. The signatures of each process were then considered to classify the multiband raster. In order to automate the processes and repeat it in subsequent analyses, a supervised Maximum Likehood Image Classification was performed. First, a training sample for each process is created and a signature file for the whole training samples was saved. This signature file can be considered valid for mapping geomorphic processes in badlands based on the specific mentioned process signatures, and the thresholds defined per each class of the input data sets.

3. MAPPING AND QUANTIFYING GEOMORPHIC PROCESSES IN BADLANDS

3.1 Study area

The study area is located in an experimental badland (0.05 km^2) located in the Soto catchment (10 km^2; Figure 2A and 2B). The Soto is a small tributary of the Upper River Cinca (8275 km^2, Central Pyrenees, Ebro Catchment, Iberian Peninsula). The main land covers of the catchment are forest (56%), badlands (26%), and field crops (18% surface). The badlands are located at an average altitude of 600 m.a.s.l. and the slope gradient can be more than 15 m with steep slopes and high degree of dissection (Figure 2A and 2B). The badlands are composed by a sequence of Eocene marls with different degrees of bedrock compactness with some few layers of sandstones. Therefore, erosional processes are hypothesised to be highly complex and spatially variable (Smith and Vericat, 2015; Figure 2B). The experimental badland in this study is described further in Smith and Vericat (2015) and at https://sites.google.com/site/badlandscan/. Specifically, the badland has a low vegetation cover (i.e. <20%), composed by isolated shrubs (e.g. *Buxus sempervirens*) on steep slopes and small groups of relatively young trees (e.g. *Pinus halepensis*) on low slopes (Figure 2A). The site has a continental climate with an annual rainfall around 700 mm. Maximum rainfall is observed during spring and autumn (e.g. maximum intensities around 47 mm h^{-1} were registered for the period 1981-2018). The average temperature is 11°C, while temperatures below freezing are often observed in winter. Figure 2B indicates some representative examples of signatures attributed to the main geomorphic processes reshaping the experimental badland.

3.2. Data

Rainfall was measured continuously by a Campbell ARG100 tipping bucket rain gauge, while air temperature was registered by means a Campbell Temperature Probe-109 (see location in Figure 2B). Both were recorded in the same a datalogger (Campbell CR200X) at a 5-minute interval.

Topographic data sets were obtained through Structure from Motion photogrammetry (SfM). Two field campaigns were performed: June 19th (S1) and December 7th 2016 (S2). Around 650 pictures per campaign were taken using a Panasonic Lumix DMC-TZ60 compact camera (focal

length 4 mm which is a 35-mm equivalent of 25 mm; 10 Mpx) mounted on a 10 m telescopic inspection pole. SfM processing was implemented using standard workflows within Agisoft Photoscan Professional 1.3.4. Dense point clouds with an average point density of around $5x10^4$ obs m^{-2} (i.e. 5 obs cm^{-2}) were obtained. Georeferencing and scaling were performed by a secondary control network of 30 Ground Control Points (GCPs) surveyed with a Leica TPS1200 Total Station (TS). The TS was set up based on a primary control network of four (fixed) benchmarks. The coordinates in each benchmark were obtained by means of a Leica Viva GS15 GNSS system and RINEX data from 3 reference stations.

3D data quality after post-processing was 0.006 m on average. Reported errors in terms of scaling and georeferencing were 0.0185 m (2.298 pixels) and 0.0222 m (1.195 pixels) for the S1 and S2 surveys, respectively. In terms of quality assessment, an independent validation dataset of 270 (S1) and 256 (S2) Check Points (ChPs) were obtained with the TS. The corresponding differences between SfM-derived point clouds and the ChPs were calculated by the M3C2 plugin (Lague et al., 2013) implemented in the open source software CloudCompare 2.6.2. Results indicated a Mean Absolute Error (i.e. MAE) of 0.0187 m (S1) and 0.0157 m (S2), and a Standard Deviation of the errors of 0.0261 m (S1) and 0.0214 m (S2).

Point clouds were filtered to remove outliers and vegetation. Outliers were filtered by means the Statistical Outlier Filter (SOR) of Cloud Compare 2.6.2 (Girardeau-Montaut, 2016), meanwhile the points located in vegetated areas were removed using the results of the supervised image classification. The open-source Topographic Point Cloud Analysis Toolkit (ToPCAT; Brasington et al., 2012; Rychkov et al., 2012) was then used to regularize the point cloud. A 0.05 x 0.05 m grid was selected taking into account the magnitude of the study area topographic changes and the size of the small geomorphic features (e.g. rills). Observations within each grid were analysed and a series of statistics of these were calculated (e.g. maximum, mean and minimum elevations and detrended standard deviation of elevations). The minimum elevation within each grid was used to represent the ground elevation within each cell. A Triangular Irregular Network or TIN was calculated based on these observations for each survey. Finally, a 0.05 m resolution DEM was computed from each TIN. The most recent DEM or DEM_{S2} was used to calculate the terrain attributes: (i) Slope, (ii) Roughness, and (iii) Concentrated Runoff Index (all inputs of MaGPiE). Following Brasington et al. (2012),

Smith and Vericat (2015) and Vericat et al. (2014), roughness was calculated using the detrended standard deviation of the elevations in each grid.

The DEMs for the two periods (DEM_{S2}-DEM_{S1}) were compared (DoD) to assess the topographic changes during the study period. The MAE of each data set was considered to represent the DEM error and the minLoD was calculated by the propagation of both DEM_{S1} and DEM_{S2} errors. Therefore, those DoD cells with absolute values below the minLoD were considered uncertain and not used in the computation of topographic changes (i.e. thresholded DoD).

For MaGPiE, the thresholds of each attribute class and the combinations between attributes and DoD classes were based on an expert-map of processes (see an example of the expert-map in Figure 1 of the Supplementary Materials section). The processes identified in the field occupied an area of 20 m^2 (represents 38% of the total area that experienced a significant topographic change during the study period, i.e. changes above the minLoD). Of this 20 m^2 area, 90% was used as a training area while 10% was used to validate the classification. Processes in this area were compared with the MaGPiE classification in order to assess the percentage of agreement between observed and MaGPiE-based process, being considered as a proxy of the accuracy of the classification.

All rasters were combined in a multiband raster data set and classified. The classification was performed based on the signatures associated with each process. The map of geomorphic process signatures (i.e. integer type raster) was transformed to a feature class (polygons). Finally, the DoD was segregated based on each geomorphic process (feature class) through the GCD ArcMap-based extension. This last step allows identification of the vertical and volumetric changes associated with each process.

3.3 Results

The study period (142 days) was characterised by a total rainfall of 355 mm distributed in 12.5 rainy days with an average intensity of 2.17 mm h^{-1}, and a maximum of 20.4 mm h^{-1}. The mean temperature was 18.2 °C, with 13 days in which the temperature reached values below 0°C with an average value of -1.4 °C and a minimum value of -4.2 °C for these days.

The thresholded DoD indicates that the majority of the area was subjected to a change below the minLoD (i.e. uncertain topographic change). Only the 8% of the total study area presents

changes above the minLoD. The spatial variability of these changes is revealed as surface lowering or erosional processes are mainly located in high slope areas, in the highest flat areas and in the main channels (76% of total area with detectable change, see Figure 3A). Conversely, surface raising or deposition is mainly located in west-facing slopes and in main channels (24 % of the total area with detectable change; Figure 3A). In terms of vertical changes, areas showing erosion have an average change of -0.06 m, while areas subjected to surface raising yield an average difference of 0.07 m (Figure 3A). Finally, the net change during the study period was -5.7 m^3 with -9.9 m^3 of erosion and 4.1 m^3 of surface raising or deposition (69% and 31% of the total volumetric changes respectively, Figure 3A).

The percentage of agreement between observed and MaGPiE-based process was around 75%, being the *Regolith Cohesion Loss* and deposition caused by *Rilling and Gullying* the more reliable signatures (i.e. 90% of agreement) and the erosion caused by *Mass wasting* the more confused signature (i.e. 60% of agreement). Figure 3B represents the DoD segregation results indicating the extension, and the vertical and volumetric changes associated to each process, while Figure 4 shows the map of main geomorphic process signatures reshaping the form of the experimental badland during the study period. Results indicate that the majority of the processes are concentrated in steep slopes, selected flat areas, and in the main channels.

Mass Wasting features, located mainly in the steepest north-facing slopes (Figure 4D), are the main geomorphic process signatures observed during the study period, both in terms of extension (54.2% of the total area with significant change) and volumetric change (47.3% of the total volumetric change; Figure 3B). These observations are in agreement with the results of Gallart et al. (2002) and Ciccacci et al. (2008), who explained that the main source of the sediments transferred from the hillslopes to channel networks in badlands developed on cohesive marls and claystones in mountain areas is via regolith falling. This gravitational process is mainly triggered by gelivation together with overlapping rainfall-driven processes (e.g. Nadal-Romero and Regüés, 2010). Regolith that was previously weathered by freeze-thaw and soil moisture changes is mobilized from steep slopes to the bottom of the main channels (see example D in Figure 4), or to small accumulation zones located at the base of the slopes near the main channel (C in Figure 4). The magnitude of these erosional processes in slopes is generally low and is likely to be below the minLoD and thus not mapped. It is

important to recognise that the omission of such low magnitude yet spatially extensive processes would bias the sediment yield estimates. The magnitude of deposition caused by *Mass Wasting* is larger, mainly due to both the accumulation of materials in small areas and the decrease in the density of the regolith after its fracture (D in Figure 4; Nadal-Romero et al., 2007). In both cases, 55% of the *Mass Wasting* geomorphic process signatures correspond to lowering or erosion while te 45% correspond to raising or deposition changes.

The second geomorphic process signature in terms of magnitude was *Sheet Washing* (25.7% of total surface and 15.8% of volumetric changes; Figure 3B). This process is mainly caused by laminar flows and rainfall drops (rainsplash) in less steep but highly exposed slopes (Figure 4B). The magnitude of *Sheet Washing* in terms of volumetric change is lower than in terms of extension (i.e. 9.9% less) due to the fact that the associated vertical changes were very low (i.e. -0.05 m on average, the process signature associated with the second-smallest vertical negative change; see B in Figure 4).

Cutting and Filling signatures were observed over 17.9% of the surface (Figure 3B) and represented the 15.6% of total volumetric change (A in Figure 4), while *Rilling and Gullying* were observed over the 8.1% of the surface of change, representing a similar volumetric change (i.e. 10.9%). Both processes are mainly caused by concentrated surface flows (runoff) but with the principal difference is that *Rilling and Gullying* was observed in steep slopes perpendicular to main channels (A in Figure 4), while *Cutting and Filling* occurred in the main channel bottoms (C in Figure 4). In terms of extension, both geomorphic process signatures presented a negative change (i.e. lowering or erosion) in more than the 85% of the surface. Finally, the signatures process that yielded the lowest magnitudes were *Regolith Cohesion Loss* (0.7% of surface and 0.3% of volumetric change with <0.05 m of surface raising on average) and the rest of combinations being considered the result of *Overlapping Processes* (0.4% of surface and 3.2% of volumetric change with 0.02 m of surface raising and -0.3 of surface lowering, on average). The low values of *Regolith Cohesion Loss* are attributed to the fact that, although freeze-thaw is considered one of the main weathering process in these landscapes, the study period was not sufficiently long to yield significant changes (i.e. only 13 days with T<0°C). Similar observations were made in Barnes et al. (2016) and Tsutsumi and Fujita (2016).

In summary, the main processes in the study badlands were both erosional and depositional processes associated to *Mass Wasting* (55% erosion and 45% deposition) and *Sheet Washing* (16% of the total volumetric change). *Cutting and Filling* (15.6%) and *Rilling and Gullying* (10.9%) were also evident processes presenting higher erosion than deposition values. These represent the key processes controlling badland evolution in the Soto catchment, yielding erosive landscapes with highly dissected shapes and high drainage densities (as observed e.g. Howard, 2009; Moreno-de las Heras and Gallart, 2018).

4. LINKING PROCESSES, SEDIMENT SOURCES AND SINKS

Several studies have tried to infer on geomorphic processes by combining landform analysis through remote sensing but at coarser resolutions than the reported here (e.g. Bartsch et al., 2002; Gude et al., 2002; Haas et al., 2016). In all cases, the most challenging task has been to establish relationships between processes and the trajectory and movement of sediment in time and space. Within this context, Sidle et al. (2019) established that hydrological and sediment connectivity is a key aspect for the parameterization of process-based models. According to Heckman et al. (2018), hydrological and sediment connectivity can be defined as the degree to which a system facilitates the transfer of water and sediment through itself, through coupling relationships between its components. The degree of connectivity in a given landscape is not static and varies over time and space due to the interaction between the external forcing (mainly precipitation and temperature), landscape properties (i.e. structural connectivity), and the magnitude of the water and sediment fluxes (i.e. functional connectivity), that will ultimately determine the frequency, distribution and magnitude of geomorphic processes (Bracken et al., 2015; Harvey, 2001; Wohl et al., 2018). Cavalli et al. (2013) developed a raster-based Index of Connectivity (IC) that quantitatively assesses the spatial distribution of structural sediment connectivity, the potential of a landscape to be connected according to its attributes; while Heckmann and Vericat (2018) presented a method to infer on the functional sediment connectivity by the computing of spatially distributed Sediment Delivery Ratios (SDR). Therefore, the approach presented here can be used to map main geomorphic process signatures and link these to the degree of connectivity to infer on source to sink trajectories at multiple spatial and temporal scales.

Figure 5 shows two examples on how the connections between geomorphic process signatures and structural and functional sediment connectivity can be further investigated. On one hand, the maps of geomorphic process signatures allow the classification of main processes acting during a given period of time (Figure 5A), while the IC maps represent the potential of a landscape to be connected in a given time (Figure 5B). A first look at the differences between both maps indicates a positive relation between IC and *Mass Wasting Erosion* and *Rilling and Gullying Erosion* processes (i.e. located in highly connected areas), while *Sheet Washing* processes are negatively related to the IC (i.e. located in disconnected areas). Lu et al. (2019) found a spatial correlation between the IC and geomorphic processes caused by overland flow, but did not find a consistent relationship with mass wasting processes. On the other hand, SDR maps (Figure 5C) permit the transfer of sediments through the landscape to be inferred alongside sediment pathways between eroding areas (i.e. source) and depositional areas (i.e. sink) and their link to main geomorphic processes triggering the flux.

5. LIMITATIONS AND CONCLUDING REMARKS

MaGPiE is based on landform attributes and topographic changes obtained from high resolution DEMs. The quality or accuracy of the map will be directly related to the resolution and precision of the DEMs. In the same way, uncertainties in the DoDs will have a direct effect, especially in landscapes like the experimental badland or during short temporal scales, in which the magnitude of observed changes may be in the range of the minLoD. In our case study, we assessed DoD uncertainty by the propagation of two uniform errors extracted from an independent network of Check Points. Although our method is widely used in the literature (e.g. Brasington et al., 2000; Lane et al., 2003; Milan et al., 2011; Wheaton et al. 2010), Anderson (2018) has recently demonstrated that net changes estimated from repeat high density observations may be affected by correlated or fully systematic errors and uncorrelated or random errors. Other more complex or complete approaches can be also applied for the assessment of uncertainties as for instance probabilistic thresholding through Fuzzy Inference Systems (e.g. Bangen et al., 2016; Wheaton et al., 2010). In the same way, more recently, James et al. (2017) presented an approach (developed in the same

experimental badland) to establish spatially variable precision maps for SfM-based surveys that enables a confidence-bounded quantification of topographic changes. In complex topography like the study area, direct 3D point cloud comparison (e.g. Lague et al., 2013) is particularly recommended.

Although the selection of the thresholds for the classes of the inputs and the different signatures or combinations were based on an expert-map-based procedure there remains a degree of uncertainty at this stage. A more objective identification of the thresholds and process signatures would be possible using Machine Learning Software such as Weka (Witten et al., 2011). Smith and Warburton (2018) previously demonstrated this machine-learning approach to select the best roughness metrics for classifying peat surfaces. In the case of MaGPiE, field observations can be used to create a training data set containing each of the main geomorphic processes which can be then used to establish the best combinations of inputs (i.e. signatures) to classify the processes.

In this technical note we have presented MaGPiE: a new algorithm that permits the mapping of geomorphic process signatures in the landscape through the analyses of repeat High Resolution Topography data sets. The method is demonstrated in an experimental badland using DEMs obtained 142 days apart. Our results indicate that MaGPiE not only allows the main geomorphic processes to be inferred, but also the evaluation of the role of each process driving the extent, vertical and volumetric changes. Through segregation of observed topographic changes the link between changes in form and geomorphic processes can be elucidated alongside evaluation of their contributions to catchment sediment yields in relation to meteorological drivers at multiple spatial and temporal scales, altogether helping in understanding landscape evolution.

Acknowledgments

This research was carried out within the framework of two research projects funded by the Spanish Ministry of Economy and Competitiveness and the European FEDER funds: MORPHSED (CGL2012-36394) and MORPHPEAK (CGL2016-78874-R). The first author has a grant funded by the Ministry of Education, Culture and Sports, Spain (FPU016/01687). The

second author is a Serra Húnter Fellow at the University of Lleida. The first and second authors are part of the Fluvial Dynamics Research Group-RIUS, a Consolidated Group recognized by the Generalitat de Catalunya (2017 SGR 459645). We also acknowledge the support of the CERCA Program of the Generalitat de Catalunya. Finally, we also thank the British Society for Geomorphology to support the long-term geomorphological monitoring program in the experimental badland that started in 2013; and the members of the Fluvial Dynamics Research Group for their assistance during the field work campaigns. We thank Prof. Stuart Lane, acting as editor in chief of the journal Earth Surface Processes and Landforms, his suggestion of considering the research paper submitted by Llena et al. (2020) where the MaGPiE algorithm is applied to a 5 years dataset and this one as a paper pair or two connected papers. Finally, we thank all comments and suggestions received from two anonymous referees and from the associate editor and the editor in chief of Earth Surface Processes and Landforms. All their comments have helped to clarify and improve this technical note.

Data availability statement

Research data not shared

Conflict of interest statement

The authors have no conflicts of interest to declare

References

Ali G, Birkel C, Tetzlaff D, Soulsby C, McDonnell JJ, and Tarolli P. 2014. A comparison of wetness indices for the prediction of observed connected saturated areas under contrasting conditions. *Earth Surface Processes and Landforms* 39: 399-413.

Anderson SW. 2018. Uncertainty in quantitative analyses of topographic change: error propagation and the role of thresholding. *Earth Surface Processes and Landforms* 44: 1015-1033.

Baade J, Franz S, Reichel A. 2012. Reservoir siltation and sediment yield in the Kruger National Park, South Africa: a first assessment. *Land Degradation and Development* 23: 586–600.

Bangen S, Hensleigh J, McHugh P, Wheaton J. 2016. Error modelling of DEMs from topographic surveys of rivers using fuzzy inference systems. *Water Resources Research* 52: 1176–1193.

Barnes N, Luffman I, Nandi A. 2016. Gully erosion and freeze-thaw processes in clay-rich soils, northeast Tennessee, USA. *GeoResJ* 9-12: 67-76.

Bartsch A, Gude M, Jonasson C, Scherer D. 2002. Identification of geomorphic process units in Kiirkevagge, northern Sweden, by remote sensing and digital terrain analysis. Geografiska Annaler 84(3-4): 171-178.

Benito G, Gutiérrez M, Sancho C. 1992. Erosion Rates in Badland Areas of the Central Ebro Basin (NE-Spain). *Catena* 19: 269-286.

Beven KJ and Kirkby MJ. 1979. A physically based, variable contributing area model of basin hydrology. *Hydrological Sciences Journal* 24(1): 43-69.

Bishop A and Morgenstern N. 1960. Stability coefficients for earth slopes. *Geotechnique* 10: 129–150.

Braken LJ, Tumbull L, Wainwright J, Bogaart P. 2015. Sediment connectivity: a framework for understanding sediment transfer at multiple scales. *Earth Surface Processes and Landforms* 40: 177–188.

Brasington J, Rumsby B, McVey R, 2000. Monitoring and Modelling Morphological Change in a Braided Gravel-Bed River Using High Resolution GPS-Based Survey. *Earth Surface Processes and Landforms* 25: 973-990.

Brasington J, Vericat D, Rychkov I. 2012. Modelling river bed morphology, roughness, and surface sedimentology using high resolution terrestrial laser scanning. *Water Resources Research*. 48: 1-18.

Bryan R, Yair A. 1982. Perspectives on studies of badland geomorphology. In: *Badland Geomorphology and Piping*, Bryan RB, Yair A (Eds.). Geobooks: Norwich; 1–12.

Buendia C, Gibbins CN, Vericat D, Batalla RJ. 2013. Reach and catchment-scale influences on invertebrate assemblages in a river with naturally high fine sediment loads. *Limnology and Ecological Management of Inland Waters* 43: 362–370.

Carrivick JL, Smith MW. 2018. Fluvial and aquatic applications of Structure from Motion photogrammetry and unmanned aerial vehicle/drone technology. *WIREs Water* 1-17.

Cavalli M, Trevisani S, Comiti F, Marchi L. 2013. Geomorphometric assessment of spatial sediment connectivity in small Alpine catchments. *Geomorphology* 188: 31–41.

Chuvieco E. 2016. *Fundamentals of Satellite Remote Sensing: An Environmental Approach*. Second edition. Taylor and Francis, USA. 468 pp.

Ciccacci S, Galiamo MC, Roma MA, Salvatore MC. 2008. Morphological analysis and erosion rate evaluation in badlands of Radicofani area (Southern Tuscany, Italy). *Catena* 74: 87–97.

Clarke ML, Rendell HM. 2010. Climate-driven decrease in erosion in extant Mediterranean badlands. *Earth Surface Processes and Landforms* 35: 1281-1288.

Clotet N, Gallart F, Sala M. 1987. Los badlands: características, interés teórico, dinámica y tasas de erosión. *Notes de Geografía Física* 15-16: 28-37.

Cossart E, Viel V, Lissak C, Reulier R, Fressard M, Delahaye D. 2018. How might sediment connectivity change in space and time? *Land Degradation and Development* 29: 2595–2613.

Cucchiaro S, Cavalli M, Vericat D, Crema S, Llena M, Beinat A, Marchi L, Cazorzi F. 2019. Geomorphic effectiveness of check dams in a debris-flow catchment using multi-temporal topographic surveys. *Catena* 174: 73-83.

Faulkner H. 2008. Connectivity as a crucial determinant of badland morphology and evolution. *Geomorphology* 100: 91-103.

Faulkner H. 2018. The Role of Piping in the Development of Badlands. In: *Badland Dynamics in the Context of Global Change*. Nadal-Romero E, Martínez-Murillo JF, Kuhn NJ. (Eds.). Elsevier, Amsterdam. 217-253.

Ferrer V, Errea P, Alonso E, Gómez-Guitierrez A, Nadal-Romero E. 2017. A Multiscale Approach to asses Geomorphological Processes in a semiarid badland area (Ebro Depression, Spain). *Cuadernos de Investigación geográfica* 43: 41-62.

Gallart F, Solé A, Puigdefàbregas J, Lázaro R. 2002. Badland Systems in the Mediterranean. In: *Dryland Rivers: Hydrology and Geomorphology of Semi-arid Channels*. Bull LJ, Kirkby MJ (Eds.). John Wiley & Sons, Ltd. 299-326.

Girardeau-Montaut D. 2019. CloudCompare - Open Source Project. http://www.danielgm.net/cc/ (accessed 01 February 2019).

Gude M, Daut G, Dietrich S, Mäusbacher R, Jonasson C, Bartsch A, Scherer D. 2002. Towards an integration of process measurements, archive analysis and modelling in geomorphology – the Kärkevagge experimental site, Abisko area, northern Sweden. Geografiska Annaler 84(3–4): 205–212.

Gutiérrez M, Sancho C, Benito G, Sirvent J, Desir G. 1997 Quantitative study of piping processes in badland áreas of the Ebro Basin, NE Spain. *Geomorphology* 20: 237-253.

Haas F, Hilger L, Neugirg F, Umstädter K, Breitung C, Fischer P, Hilger P, Heckman T, Dusik J, Kaiser A, Schmidt J, Della Seta M, Rosenkranz R, Becht M. 2016. Quantification and analysis of geomorphic processes on a recultivated iron ore mine on the Italian island of Elba using long-term ground-based lidar and photogrammetric SfM data by a UAV. *Natural Hazards and Earth System Sciences* 16: 1269-1288.

Harvey, A.M., 2001. Coupling between hillslopes and channels in upland fluvial systems: implications for landscape sensitivity, illustrated from the Howgill Fells, northwest England. *Catena* 42: 225–250.

Heckmann, T, Vericat D. 2018. Computing spatially distributed sediment delivery ratios: inferring functional sediment connectivity from repeat high-resolution digital elevation models. *Earth Surface Processes and Landforms*. 43: 1547–1554.

Howard AD. 2009. Badlands and gullying. In: *Geomorphology of Desert Environments*. Parsons AJ, Abrahams AD. (Eds.). Springer, Berlin. 265–299.

Huggett RJ. 2011. *Fundamentals of Geomorphology*, 3rd edition. Routledge, New York. 533 pp.

James MR, Robson S, Smith, MW. 2017. 3-D uncertainty-based topographic change detection with structure-from-motion photogrammetry: precision maps for ground control and directly georeferenced surveys. *Earth Surface Processes and Landforms* 42: 1769–1788.

Jancewicz K, Migon P, Kasprzak M. 2019. Connectivity patterns in contrasting types of tableland sandstone relief revealed by TopographicWetness Index. *Science of the Total Environment* 656: 1046-1062.

Kasanin-Grubin M. 2013. Clay mineralogy as a crucial factor in badlands hillslope processes. *Catena* 106: 54–67.

Lague D, Brodu N, Leroux J. 2013. Accurate 3D comparison of complex topography with terrestrial laser scanner: Application to the Rangitikei canyon (N-Z). *ISPRS Journal of Photogrammetry and Remote Sensing* 82: 10-26.

Lane SN, Westaway RM, Hicks M. 2003. Estimation of erosion and deposition volumes in a large, gravel bed, braided river using synoptic remote sensing. *Earth Surface Processes and Landforms* 28: 249-271.

Llena M, Smith MW, Wheaton JM, Vericat D. 2020. Geomorphic process signatures reshaping sub-humid Mediterranean badlands: 2. Application to 5 years dataset. *Earth Surface Processes and Landforms.* This issue.

López-Tarazón JA, Batalla RJ, Vericat D, Francke T. 2012. The sediment budget of a highly dynamic mesoscale catchment: the river Isábena. *Geomorphology* 138: 15–28.

Lu X, Li Y, Washington-Allen RA, Li Y. 2019. Structural and sedimentological connectivity on a rilled hillslope. *Science of Total Environment* 655: 1479-1494.

Martínez-Casasnovas JA, Poch RM. 1998. Estado de conservación de los suelos d ela cuenca del embalse Joaquín Costa. *Limnética* 14: 83-91.

Mathys N, Brochot S, Meunier M. 1996. Erosion of the Terres Noires (Black Earth) in the southern French Alps : A contribution to an assessment of mean annual values (Draix experimental catchment areas). *Revue de géographie alpine* 84 (2): 17-27.

Milan DJ, Heritage GL, Large ARG, Fuller IC. 2011. Filtering spatial error from DEMs: Implications for morphological change estimation. *Geomorphology* 125: 160–171.

Moreno-de las Heras M, Gallart F. 2018. The Origin of Badlands. In: *Badland Dynamics in the Context of Global Change*. Nadal-Romero E, Martínez-Murillo JF, Kuhn NJ. (Eds.). Elsevier, Amsterdam. 27-59.

Morgenstern N. 1965. The analysis of the stability of general slip surfaces. *Geotechnique* 15(1): 79–93.

Mueller EN, Güntner A, Francke T, Mamede G. 2010. Modelling sediment export, retention and reservoir sedimentation in drylands with the WASA-SED model. *Geoscientific Model Development* 3: 275-291.

Nadal-Romero E, Regüés D, Martí-Bono C, Serrano-Muela P. 2007. Badland dynamics in the Central Pyrenees: temporal and spatial patterns of weathering processes. *Earth Surface Processes and Landforms* 32: 888-904.

Nadal-Romero E, Regüés D. 2010. Geomorphological dynamics of sub-humid mountain badland areas: weathering, hydrological and suspended sediment transport processes. A case of study in the Araguás catchment (Central Pyrenees), and implications for altered hydro-climatic regimes. *Progress in Physical Geography* 34 (3): 123–150.

Nadal-Romero E, Revuelto J, Errea P, López-Moreno JI. 2015. The application of terrestrial laser scanner and SfM photogrammetry in measuring erosion and deposition processes in two opposite slopes in a humid badlands area (central Spanish Pyrenees). *SOIL* 1, 561–573.

Nadal-Romero E, García-Ruiz JM. 2018. Rethinking Spatial and Temporal Variability of Erosion in Badlands. In: *Badland Dynamics in the Context of Global Change*. Nadal-Romero E, Martínez-Murillo JF, Kuhn NJ. (Eds.). Elsevier, Amsterdam. 217-253.

Neugirg F, Stark M, Kaiser A, Vlacilova M, Della Seta M, Vergari F, Schmidt J, Becht M, Haas F. 2016. Erosion processes in calanchi in the Upper Orcia Valley, Southern Tuscany, Italy based on multitemporal high-resolution terrestrial LiDAR and UAV surveys. *Geomorphology* 269: 8–22.

Nobajas A, Waller RI, Robinson ZP, Sangonzalo R. 2017. Too much of a good thing? the role of detailed UAV imagery in characterizing large-scale badland drainage characteristics in South-Eastern Spain. *International Journal of Remote Sensing* 38: 2845-2860.

Passalacqua P, Belmont P, Staley DM, Simley JD, Arrowsmith JR, Bode CA, Crosby C, DeLong SB, Glenn NF, Kelly SA, Lague D, Sangireddy H, Schaffrath K, Tarboton DG, Wasklewicz T, Wheaton JM. 2015. Analyzing high resolution topography for advancing the understanding of mass and energy transfer through landscapes: a review. *Earth-Science Reviews* 148: 174-193.

Piqué G, López-Tarazón JA, Batalla RJ. 2014. Variability of in-channel sediment storage in a river draining highly erodible areas (the Isábena, Ebro basin). *Journal Soils Sediments* 12: 2031-2044.

Regüés D, Pardini G, Gallart F. 1995. Regolith behaviour and physical weathering of clayey mudrock as dependent on seasonal weather conditions in a badland area at Vallcebre, Eastern Pyrenees. *Catena* 25: 199-212.

Regüés D, Guàrdia R, Gallart F. 2000. Geomorphic agents versus vegetation spreading as causes of badland occurrence in a Mediterranean subhumid mountainous area. *Catena* 40(2): 173–187.

Regüés D, Torri D. 2002. Efecto de la energía cinética de la lluvia sobre la dinámica de las propiedades físicas y el encostramiento en un suelo arcilloso sin vegetación. *Cuaternario y Geomorfología* 16: 57–71.

Roering JJ, Kirchner JW, Dietrich WE. 2001. Hillslope evolution by nonlinear, slope-dependent transport: steady-state morphology and equilibrium adjustment timescales. *Journal of Geophysical Research* 106: 16499–16513.

Römkens MJM, Helming K. Prasad SN. 2002. Soil erosion under different rainfall intensities, surface roughness, and soil water regimes. *Catena* 46(2-3): 103-123.

Rychkov I, Brasington J, Vericat D. 2012. Computational and methodological aspects of terrestrial surface analysis based on point clouds. *Computers & Geosciences* 42: 64-70.

Sidle RC, Jarihani B, Kaka SI, Koci J, Al-Shaibani A. 2019. Hydrogeomorphic processes affecting dryland gully erosion: Implications for modelling. *Progress in Physical Geography* 43(1): 46-64.

Sirvent J, Desir G, Gutierrez M, Sancho C, Benito G. 1997. Erosion rates in badland areas recorded by collectors, erosion pins and profi lometer techniques (Ebro Basin, NE-Spain). *Geomorphology* 18: 61–75.

Smith, MW, Carrivick, JL, and Quincey, DJ 2015. Structure from Motion photogrammetry in physical geography. *Progress in Physical Geography* 40(2): 247-275.

Smith MW, Vericat D. 2015. From experimental plots to experimental landscapes: topography, erosion and deposition in sub-humid badlands from Structure-from-motion photogrammetry. *Earth Surface Processes and Landforms* 40: 1656-1671.

Smith MW, Warburton J. 2018. Microtopography of bare peat: a conceptual model and objective classification from high-resolution topographic survey data. *Earth Surface Processes and Landforms* 43: 1557-1574.

Stöcker C, Eltner A, Karrasch P. 2015. Measuring gullies by synergetic application of UAV and close range photogrammetry — a case study from Andalusia, Spain. *Catena* 132: 1–11.

Tarolli, P. 2014. High-resolution topography for understanding Earth surface processes: opportunities and challenges. *Geomorphology* 216: 295–312.

Torri D, Calzolari C, Rodolfi G. 2000. Badlands in changing environments: An introduction. *Catena* 40: 119–125.

Tsutsumi D, Fujita M. 2016. Field observations, experiments, and modeling of sediment production from freeze and thaw action on a bare, weathered granite slope in a temperate region of Japan. *Geomorphology* 267: 37-47.

Vergari F, Troiani F, Faulkner H, Del Monte M, Della Seta M, Ciccacci S, Fredi P. 2019. The use of the slope-area function to analyse process domains in complex badland landscapes. *Earth Surface Processes and Landforms* 44: 273-286.

Vericat D, Smith MW, Brasington J. 2014. Patterns of topographic change in sub-humid badlands determined by high resolution multi-temporal topographic surveys. *Catena* 120: 164–176.

Vericat D, Wheaton J, Brasington J. 2017. Revisiting the Morphological Approach: Opportunities and Challenges with Repeat High-Resolution Topography. In: *Gravel-Bed Rivers: Processes and Disasters*. Tsutsumi DT, Laronne JB. (Eds.). Wiley, 121-158.

Westoby MJ, Brasington J, Glasser NF. 2012. 'Structure-from-motion' photogrammetry: a low-cost, effective tool for geoscience applications. *Geomorphology* 179: 300–314.

Wheaton JM, Brasington J, Darby SE, Sear DA. 2010. Accounting for uncertainty in DEMs from repeat topographic surveys: improved sediment budgets. *Earth Surface Processes and Landforms* 35(2): 136–156.

Wheaton JM, Brasington J, Darby SE, Kaspark A, Sear D, Vericat D. 2013. Morphodynamic signatures of braiding mechanisms as expressed through change in sediment storage in a gravel-bed river. *Journal of Geophysical Research: Earth Surface* 118: 759-779.

Willgoose GR, Bras RL, Rodriguez-Iturbe I. 1991. A coupled channel network growth and hillslope evolution model. *Water Resources Research* 27: 1671–1702.

Williams JG, Rosser NJ, Hardy RJ, Brain MJ, Afana AA. 2018. Optimising 4-D surface change detection: an approach for capturing rockfall magnitude-frequency. *Earth Surface Dynamics* 6: 101–119.

Witten IH, Frank E, Hall MA. 2011. *Data Mining: Practical Machine Learning Tools and Techniques*, 3rd edn. Burlington USA: Morgan Kaufmann.

Wohl E, Brierley G, Cadol D, Coulthard TJ, Covino T, Fryirs KA, Grant G, Hilton RG, Lane SN, Magilligan FJ, Meitzen KM, Passalacqua P, Poeppl RE, Rathburn SL, Sklar LS. 2018. Connectivity as an emergent property of geomorphic systems. *Earth Surface Processes and Landform* 44:4-26

Yair A, Lavee H, Bryan RB, Adar E. 1980. Runoff and erosion processes and rates in the Zin Valley badlands, Northern Negev, Israel. *Earth Surface Processes* 5: 205-225.

Zhang FB, Yang MY, Li BB, Li ZB, Shi WY. 2017. Effects of slope gradient on hydro-erosional processes on an aeolian sand-covered loess slope under simulated rainfall. *Journal of Hydrology* 553: 447-456.

Table 1. Key geomorphic processes in badlands in relation to the main drivers and according to previous literature and field observations.

Geomorphic process	Description	Main drivers	References
Sheet Washing	Uniform erosion of soil in thin superficial layers.	Laminar surface runoff (overland flow) and rainsplash	Gallart et al., 2002; Nadal-Romero and García-Ruiz, 2018
Rilling and Gullying	Shallow channels cut into hillside soil or soft rock outcrops. Smaller incised channels are considered rills while larger channels are known as gullies.	Concentrated surface runoff (overland flow)	Clotet et al., 1987; Moreno-de las Heras and Gallart, 2018
Cutting and Filling	Fluvial processes that take place in the main channel bottom with relatively low slope and higher section width in comparison with the rest of the drainage network.	Concentrated surface runoff (overland flow)	Clotet et al., 1987; Gallart et al., 2002
Mass Wasting	Caused by regolith slope mass movements (falling) produced after its destabilization.	Freeze-thaw (winter), wetting-drying cycles and rainsplash	Barnes et al., 2016; Nadal-Romero and Regües 2010
Regolith Cohesion Loss	Surface raising caused by the fracture or expansion of the superficial regolith.	Freeze-thaw (winter) and wetting-drying cycles	Barnes et al., 2016; Nadal-Romero and Regües 2010
Overlapping Processes	Geomorphic processes that interact/overlap and it is not possible to infer from the signatures based on landform attributes and changes in form. In the study area the main overlapped process signatures are Sheet Washing and Regolith Cohesion Loss in exposed flat areas.	Interaction of different drivers	Vergari et al., 2019

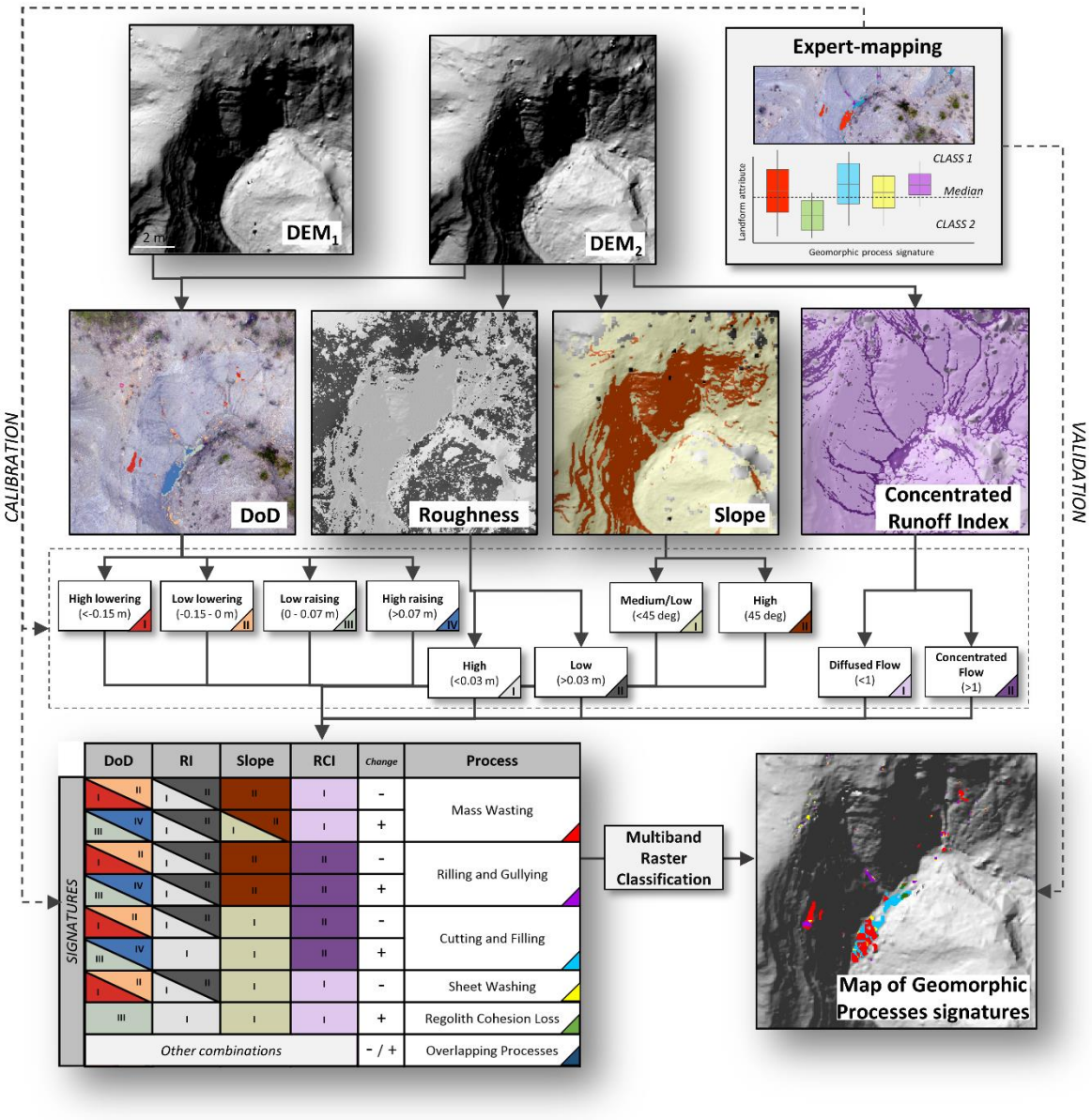

Figure 1. The MaGPiE GIS-based decision tree algorithm used to obtain Maps of Geomorphic Process Signatures in sub-humid badlands. Note that the algorithm was developed to map the signatures of the main processes observed in sub-humid Badlands but it can be modified according to other landscapes as discussed in the text. *Overlapping Processes* are considered those yielding a distinct signature to the other identified processes, being not able to be classified.

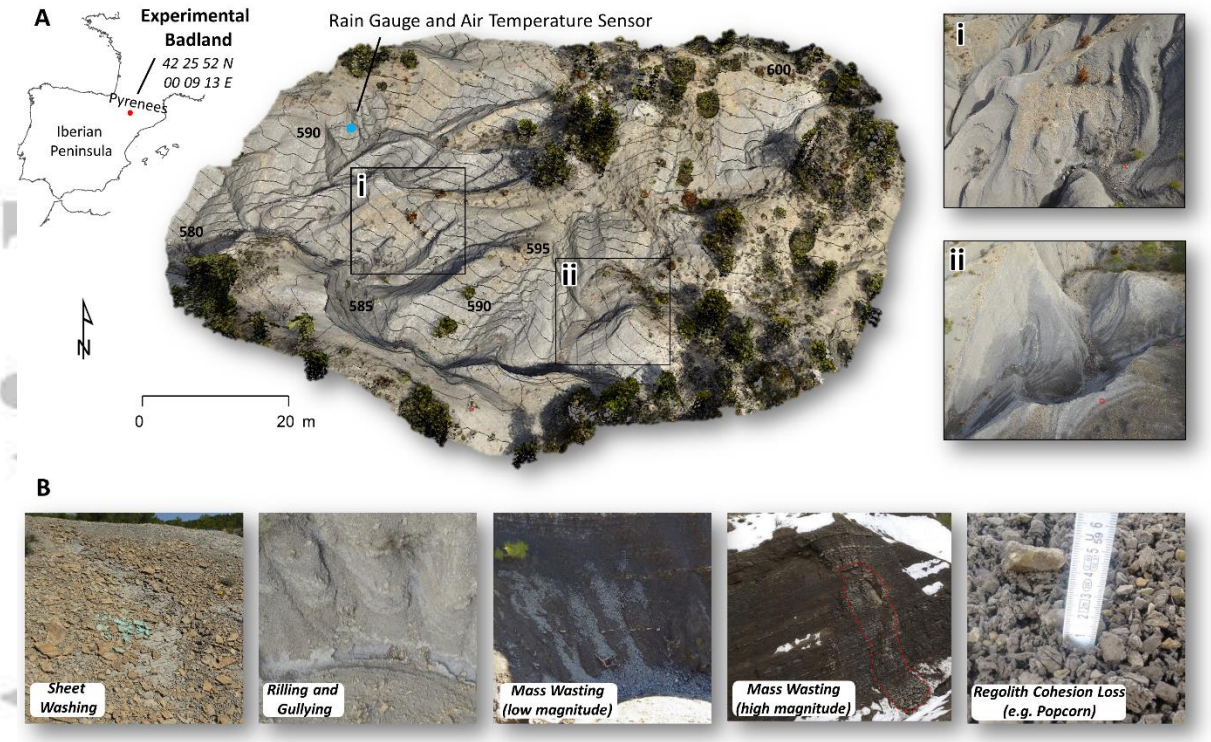

Figure 2. A. Location of the Experimental Badland (red dot) and Photo-rendered point cloud of the targeted Badland with 2 close up photo views (i and ii). Note that contour lines with an equidistance of 1 m are also shown on it. The blue dot indicates the location of both the Rain Gauge and Temperature Sensor. B. Examples of the signatures of main geomorphic processes observed in the experimental badland.

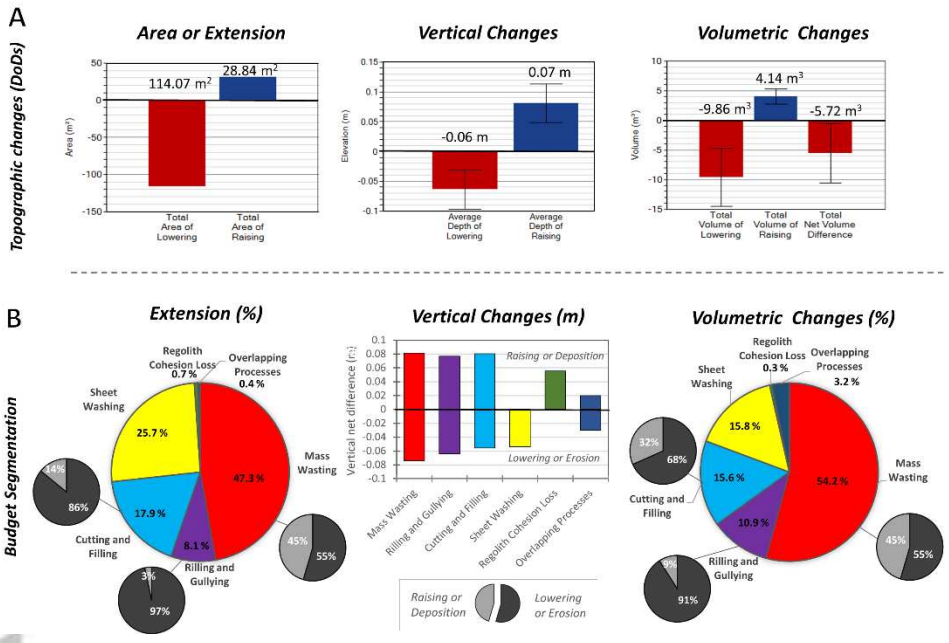

Figure 3. A. Topographic changes in the Experimental Badland for the period July 2016 (S1) to December 2016 (S2) expressed in terms of areal extent (m^2), vertical (m) and volumetric (m^3) changes. Note that the coloured bars represent the average values and the error bars show the possible variation (+/-) related to the propagated error. Average values are also presented above each bar. B. DoD segregation results of experiencing changes areas based on mapped geomorphic processes: areal extension of each process (%), mean vertical differences (m), and volumetric differences expressed in percentage (%).

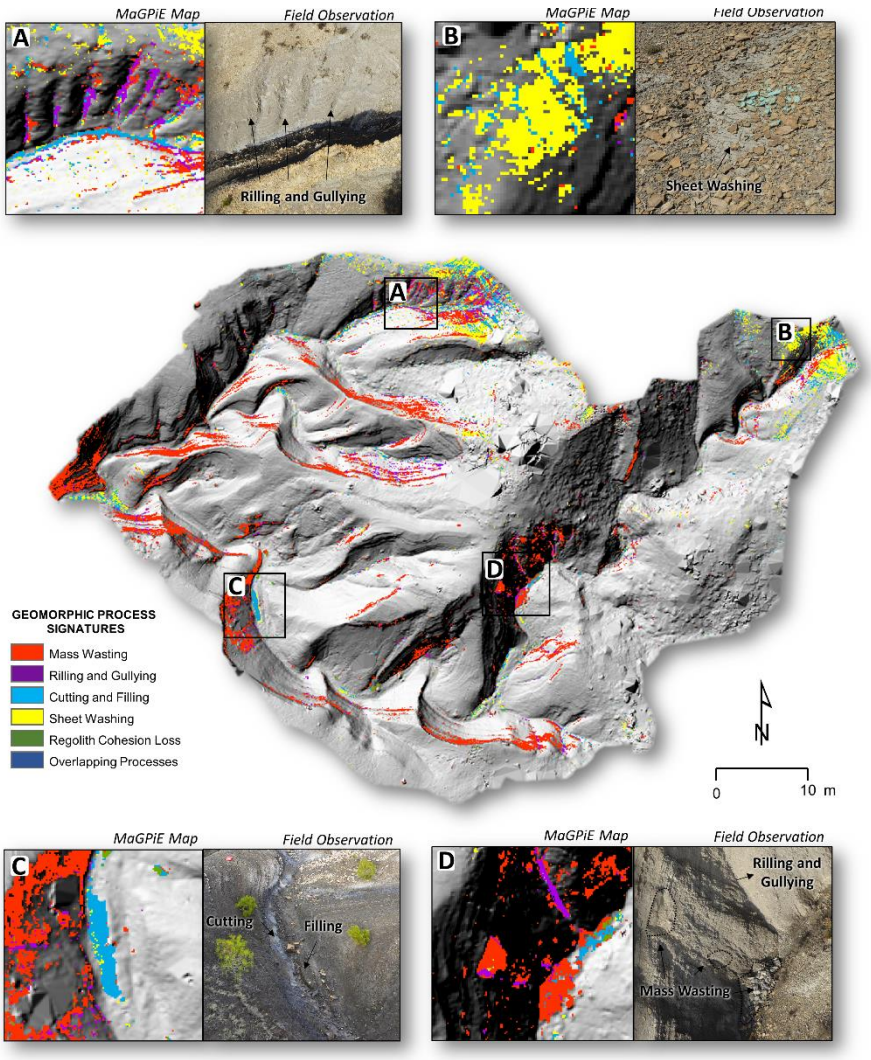

Figure 4. Map of geomorphic processes in the experimental badland for the period July 2016 (S1) to December 2016 (S2) with selected examples of field observations of processes in close agreement with the MaGPiE outputs (A-D). Note that the extension of the Field Observation did not fully match with the extent of the MaGPiE Map zoom due to it corresponds to oblique photography taken form the ground.

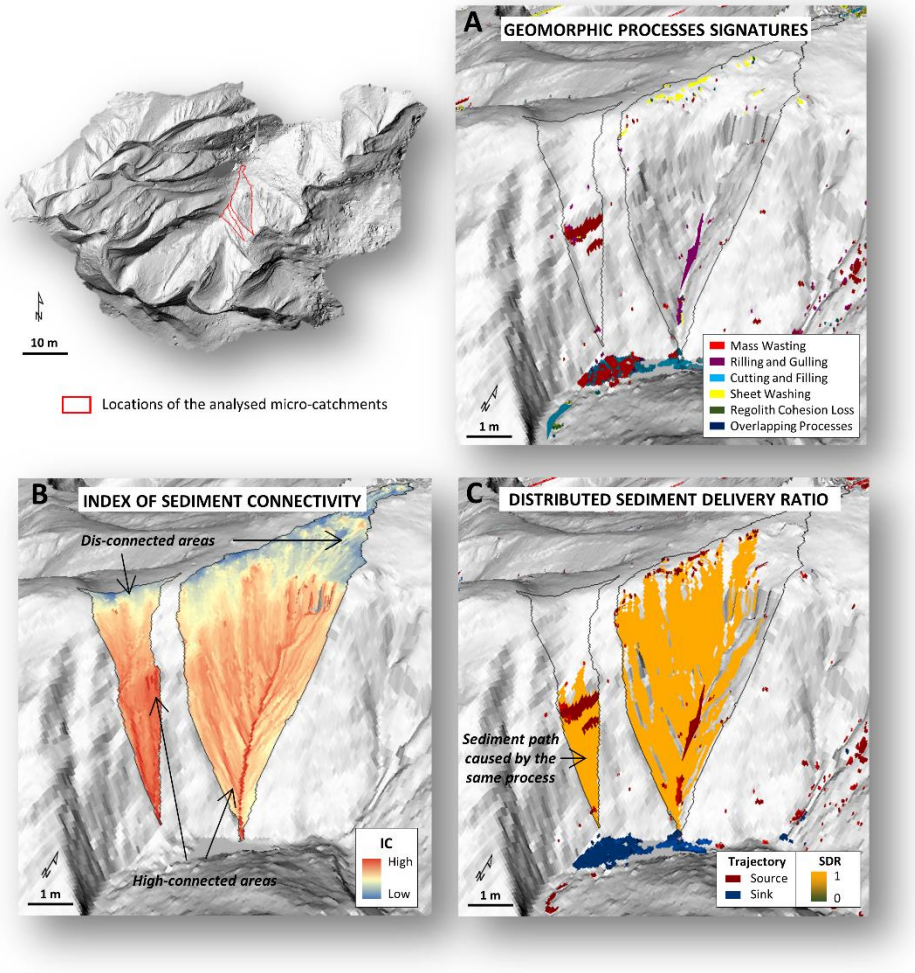

Figure 5. Inferring the connections between Geomorphic Process Signatures and structural and functional sediment connectivity for two representative micro-catchments of the study badlands. A. Geomorphic Process Signatures map obtained from the application of the MaGPiE algorithm. B. Map of Index of Sediment Connectivity (IC) developed by Cavalli et al. (2013). C. Spatial Distributed Sediment Delivery Ratio (SDR) computed by the method presented by Heckmann and Vericat (2018). Note that the erosion and deposition features are also shown as indicative of source and sink of sediment trajectories respectively.

Geomorphic process signatures reshaping sub-humid Mediterranean badlands: 1. Methodological development based on High Resolution Topography

Llena, M.*, Vericat, D., Smith, M.W., Wheaton, J.M.

Key findings:

- This paper presents a new algorithm (MaGPiE) to map geomorphic processes signatures through the analyses of repeat High Resolution Topography data sets.
- MaGPiE is a GIS-based algorithm that requires as input landscape attributes and a map of topographic changes.
- MaGPiE allows inferring in the magnitude and the spatial distribution of the main geomorphic processes reshaping badlands.

Representative figure: